Quantum Spin Hall State on Square-like Lattice

Zhida Song,[1] S. M. Nie,[1] Hongming Weng,[1,2,*] and Zhong Fang[1,2,†]

[1]*Beijing National Laboratory for Condensed Matter Physics,*

and Institute of Physics, Chinese Academy of Sciences, Beijing 100190, China

[2]*Collaborative Innovation Center of Quantum Matter, Beijing, 100084, China*

(Dated: August 24, 2015)

Abstract

We find that quantum spin Hall (QSH) state can be obtained on a square-like or rectangular lattice, which is generalized from two-dimensional (2D) transition metal dichalcogenide (TMD) haeckelites. Band inversion is shown to be controled by hopping parameters and results in Dirac cones with opposite or same vorticity when spin-orbit coupling (SOC) is not considered. Effective k·p model has been constructed to show the merging or annihilation of these Dirac cones, supplemented with the intuitive pseudospin texture. Similar to graphene based honeycomb lattice system, the QSH insulator is driven by SOC, which opens band gap at the Dirac cones. We employ the center evolution of hybrid Wannier function from Wilson-loop method, as well as the direct integral of Berry curvature, to identify the Z_2 number. We hope our detailed analysis will stimulate further efforts in searching for QSH insulators in square or rectangular lattice, in addition to the graphene based honeycomb lattice.

1

I. INTRODUCTION

Topological insulator (TI) has attracted significant attentions from researchers in recent years.[1–4] Its bulk band structure is characterized by a global topological invariant $\mathbb{Z}_2$ number,[5–9] which is protected by time-reversal (TR) symmetry. The bulk-boundary correspondence ensures that on the boundary of a TI there exists topologically protected metallic states which cross the bulk band gap by connecting the valence and conduction bands. Especially for two dimensional (2D) TI, the conducting one dimensional (1D) edge states have opposite velocity for opposite spin channel, which leads to quantum spin Hall (QSH) effect. Therefore, 2D TI is also known as QSH insulator. Since the backscattering of electrons in this 1D edge state is prohibited as long as TR symmetry is conserved, dissipationless quantized electron conductivity is expected and has great potential application as an ideal conducting wire in device.

However, up to now, only two materials have been confirmed by experimental observation of quantized conductivity inside of bulk band gap, namely, the quantum well structure composed of HgTe/CdTe[10] and InAs/GaSb.[11] There have been intensive efforts in searching for 2D QSH insulator. One is based on the honeycomb lattice, which is stimulated by Kane-Mele model for graphene.[5,12] The low-buckled silicene[13], chemically decorated single layer honeycomb lattice of Sn,[14] Ge[15] and Bi or Sb[16] are all in this category. The second category is represented by $ZrTe_5$/$HfTe_5$[17] and Bi_4Br_4[18]. They are single layer exfoliated from their three-dimensional (3D) counterparts, which are weakly bonded layered materials. The proposal of 1T' structure of single layer transition-metal dichalcogenide (TMD)[19] can be ascribed to this type also. The third category are based on square or rectangular lattice. Such as recent proposals of 2D buckled square lattice BiF[20] and rectangular TMD haeckelites.[21–23]

In this work, we will discuss the possible topologically nontrivial quantum states based on the model built for 2D monolayer transition metal dichalcogenide (TMD) haeckelites,[24,25] among which MX_2 (M=Mo, W and X=S, Se, Te) have been predicted to be QSH insulators by Nie et $al.$[21], Sun et $al.$[22] and Ma et $al.$[23] using first-principles calculations.

The paper is organized as follows. In section II,the effective tight-binding (TB) model of TMD haeckelites are constructed from symmetrical analysis. In section III, the symmetry and topology of the lattice model and the topological phase transition have been discussed. In section IV, the vorticity, merging or annihilation of Dirac cones have been demonstrated

by k·p model. In section V, we provide a brief summary.

II. DERIVATION OF TIGHT BINDING MODEL

Monolayer of TMD in its top view, such as MoS_2, can be thought as a honeycomb lattice with Mo and S on the A and B sublattice site, respectively. However, recently a kind of ordered square-octagonal distortion have been introduced in honeycomb TMD to form haeckelite structure[24,25] as that in graphene. Such TMD haeckelites have pairs of square-octagon composed of M and X atoms, noted as MX_2-4-8 to be distinguished from usual MX_2 with honeycomb lattice. In our previous work[21], the first-principles calculation for WS_2-4-8 indicates the four bands around the Fermi level are mainly contributed by d_{z^2} orbitals of M atoms. The p orbitals from X atoms are quite far from Fermi level and can be safely ignored. In this point of view, the square-octagonal lattice can be further simplified to be a rectangular lattice with only four M atoms per unit cell as shown in Fig. 1.

A. Hamiltonian without SOC Term

We take d_{z^2} orbital on each M atom as local orbital basis and note it as Wannier orbital $w_n(\boldsymbol{r} - \boldsymbol{R}_l)$. Here $n=1...4$ indicates four nonequivalent M atoms in one unit cell as shown in Fig. 1 and $\boldsymbol{R}_l$ is the lattice index. Such rectangular lattice has space group $Pbam$ and the following symmetries are satisfied.

$\mathcal{P}$: inversion symmetry operator. M_1 (M_2) and M_3 (M_4) are related by $\mathcal{P}$.

m_z: mirror operator with mirror plane perpendicular to normal of the 2D lattice plane. All M atoms keep identity.

$\{C_{2x}|\frac{1}{2}\frac{1}{2}0\}$: This is a non-symmorphic operation. After C_2 rotation around x-axis (along a lattice), a glide of $(\frac{1}{2}, \frac{1}{2}, 0)$ (in unit of lattice vectors) is applied. This operation relates M_1 (M_3) with M_2 (M_4).

Therefore, there are only three independent hopping terms in tight-binding (TB) approximation and they are:

$$t_1 = \langle w_1 | H_0 | w_2 \rangle \tag{1}$$

$$t_2 = \langle w_1 | H_0 | w_{3t} \rangle \tag{2}$$

$$t_3 = \langle w_1 | H_0 | w_4 \rangle \tag{3}$$

Here H_0 is the Hamiltonian of system without considering of spin-orbit coupling (SOC). The hopping parameters t_1, t_2 and t_3 are marked in Fig. 1 also. All these parameters must be real because w_n and H_0 are real. After fourier transformation $H_{0nm}(\boldsymbol{k}) = \sum_{\boldsymbol{R}} \langle w_n(0) | H_0 | w_m(\boldsymbol{R}) \rangle e^{i \boldsymbol{k} \cdot \boldsymbol{R}}$, we get $\boldsymbol{k}$ dependent Hamiltonian $H_0(\boldsymbol{k})$ satisfying periodic condition $H_0(\boldsymbol{k}) = H_0(\boldsymbol{k} + \boldsymbol{G})$ with $\boldsymbol{G}$ being integer times of reciprocal lattice. A $\mathbf{k}$-dependent gauge transformation $H_0(\boldsymbol{k}) \rightarrow U(\boldsymbol{k}) H_0(\boldsymbol{k}) U^\dagger(\boldsymbol{k})$ is applied to get a concise but not periodic form of $H_0(\boldsymbol{k})$ in Eq. (4). This form is more convenient for deriving the effective k·p models used in section IV.

$$H_0(\boldsymbol{k}) = \begin{pmatrix} 0 & \gamma_1 & \gamma_2^- & \gamma_3 \\ \gamma_1^* & 0 & \gamma_3^* & \gamma_2^+ \\ \gamma_2^{-*} & \gamma_3 & 0 & \gamma_1 \\ \gamma_3^* & \gamma_2^{+*} & \gamma_1^* & 0 \end{pmatrix} \tag{4}$$

$$\gamma_1 = 2t_1 \cos\left(\frac{k_x}{2}\right)$$

$$\gamma_2^\pm = t_2 e^{-i\frac{1}{2}(k_x \pm k_y)}$$

$$\gamma_3 = 2t_3 \cos\left(\frac{k_y}{2}\right)$$

$$U(\boldsymbol{k}) = \begin{pmatrix} 1 & 0 & 0 & 0 \\ 0 & e^{-\frac{i}{2}k_x} & 0 & 0 \\ 0 & 0 & e^{-\frac{i}{2}(k_x + k_y)} & 0 \\ 0 & 0 & 0 & e^{-\frac{i}{2}k_y} \end{pmatrix} \tag{5}$$

B. Spin-Orbit Coupling Terms

To include SOC term, the degree of freedom of spin is introduced explicitly to expand the dimension of the Hamiltonian from four to eight. The spinor basis set is defined as:

$$|\phi_i\rangle = w_i(\boldsymbol{r}) \otimes \chi_\uparrow \quad i = 1 \cdots 4 \tag{6}$$

$$|\phi_{i+4}\rangle = w_i(\boldsymbol{r}) \otimes \chi_\downarrow \quad i = 1 \cdots 4 \tag{7}$$

, where $\chi_\uparrow = (1,0)^T$ and $\chi_\downarrow = (0,1)^T$ with T representing transpose. Correspondingly, all the above symmetrical operators should be adjusted:

$$\mathcal{P} \rightarrow \mathcal{P}$$

$$m_z \rightarrow m_z e^{-\frac{i}{2}\pi\sigma_z}$$

$$\left\{ C_{2x} \Big| \frac{1}{2}\frac{1}{2}0 \right\} \rightarrow \left\{ C_{2x} \Big| \frac{1}{2}\frac{1}{2}0 \right\} e^{-\frac{i}{2}\pi\sigma_x}$$

and TR operator is defined as $\mathcal{T} = -i\sigma_y K$ with K is complex conjugation operator. Considering these symmetrical constraints, we will derive the term including SOC H_{so}.

Mirror symmetry m_z. Similar as the case in Kane-Mele model[12] on honeycomb lattice without Rashba term, H_{so} for present TMD haeckelite is also block diagonal in spin space because of m_z symmetry. This can be proved as:

$$\forall i, j = 1 \cdots 4$$

$$\langle \phi_{i+4} | H_{so} | \phi_j \rangle = \langle m_z e^{-\frac{i}{2}\pi\sigma_z} \phi_{i+4} | H_{so} | m_z e^{-\frac{i}{2}\pi\sigma_z} \phi_j \rangle$$

$$= -\langle \phi_{i+4} | H_{so} | \phi_j \rangle = 0$$

The derivation from the second line to the third line is due to $e^{-\frac{i}{2}\pi\sigma_z} = -i\sigma_z$.

Time-reversal symmetry $\mathcal{T}$. $H_{so}^{\uparrow\uparrow}$ and $H_{so}^{\downarrow\downarrow}$ are related by $\mathcal{T}$:

$$\langle \phi_{i+4} | H_{so} | \phi_{j+4} \rangle = \langle \mathcal{T}\phi_i | H_{so} | \mathcal{T}\phi_j \rangle$$

$$= \langle \phi_j | H_{so} | \phi_i \rangle \tag{8}$$

i.e., $H_{so}^{\uparrow\uparrow} = H_{so}^{\downarrow\downarrow T}$.

Inversion symmetry $\mathcal{P}$ and combined symmetry $\left\{ C_{2x} \Big| \frac{1}{2}\frac{1}{2}0 \right\} e^{-\frac{i}{2}\pi\sigma_x} \cdot \mathcal{T}$. These two operations do not flip spin. After an intuitive graphic analysis as illustrated in Fig. 1, one can

easily find that there are only two independent non-zero parameters:

$$\langle\phi_1|H_{so}|\phi_2\rangle = \langle\phi_3|H_{so}|\phi_4\rangle = i\lambda_1 \tag{9}$$

$$\langle\phi_1|H_{so}|\phi_4\rangle = \langle\phi_3|H_{so}|\phi_2\rangle = i\lambda_3 \tag{10}$$

Note that these two SOC terms must be pure imaginary numbers because ϕ_i are real and H_{so} contains an imaginary unit. We also note that $\langle\phi_1|H_{so}|\phi_{3t}\rangle$ must be zero because $\mathcal{P}$ transforms it to its complex conjugation.

Therefore, H_{so} is always diagonal in spin space and $\mathcal{PT}$ guarantees spin degeneracy, i.e., Kramer degeneracy. We only need to deal with $H_{so}^{\uparrow\uparrow}$ for the rest of this article. The concise matrix form of H_{so} in Eq. (11) is achieved by the same gauge transform (Eq. (5)) performed to one spin channel of $H_{so}(\boldsymbol{k})$.

$$H_{so}^{\uparrow\uparrow}(\boldsymbol{k}) = \begin{pmatrix} 0 & \delta_1 & 0 & \delta_3 \\ \delta_1^* & 0 & \delta_3^* & 0 \\ 0 & \delta_3 & 0 & \delta_1 \\ \delta_3^* & 0 & \delta_1^* & 0 \end{pmatrix} \tag{11}$$

$$\delta_1 = 2i\lambda_1 \cos\left(\frac{k_x}{2}\right)$$

$$\delta_3 = 2i\lambda_3 \cos\left(\frac{k_y}{2}\right)$$

Now we get the total effective TB model $H(\boldsymbol{k})=H_0(\boldsymbol{k}) + H_{so}(\boldsymbol{k})$, but keep in mind that the periodic condition is sacrificed to get the conciseness in Eq. (4) and Eq. (11), and a gauge transformation (Eq. (5)) to periodic form is needed when calculating properties concerning global phase such as Berry phase and related properties.

III. SYMMETRY AND TOPOLOGY OF THE BANDS

From the analysis of symmetry in the above section, we obtain a TB model as shown in Eq. (4) and Eq. (11). We now focus on the band structure and the topology with different choice of related parameters. In real materials, these parameters are determined by details in crystal structure and choice of M and X elements in MX$_2$-4-8 haeckelites.[21] It should be noticed that only the sign$(t_1 t_2 t_3)$ makes sense. This can be easily understood if we can use some unitary transformation UHU^T to change t_i's signs in pairs. For example, $U=\mathbb{I}_2 \otimes \tau_z$
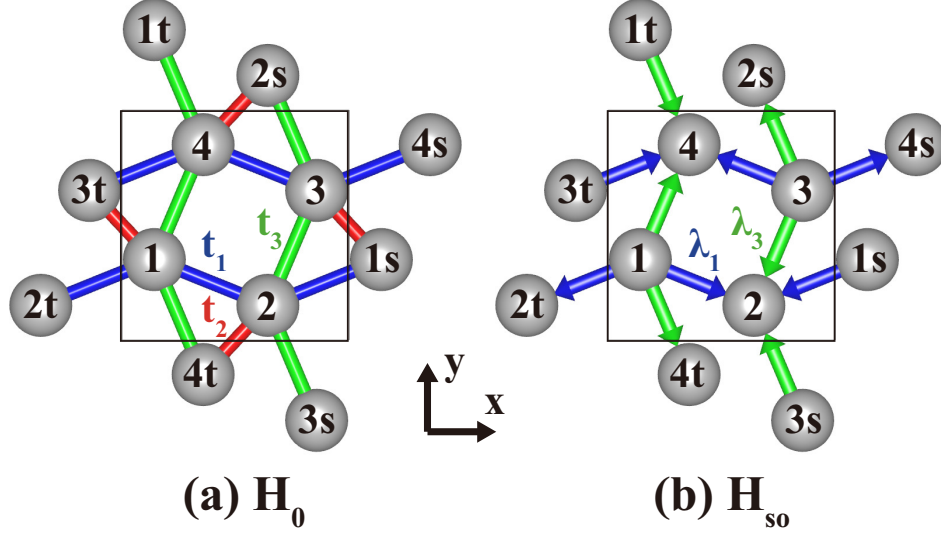
FIG. 1: 2D rectangular lattice with four sties per cell. (a) Hopping parameters t_1, t_2 and t_3 in H_0. (b) Finite parameters λ_1 and λ_3 in H_{so} with each arrow points from bra to ket.

transforms t_1, t_3 to $-t_1$, $-t_3$ and $U=\tau_z \otimes \mathbb{I}_2$ transforms t_2, t_3 to $-t_2$, $-t_3$. The change in the sign($t_1 t_2 t_3$), whatever which sign(t_i) changes, is equivalent to $H_0(\boldsymbol{k}) \rightarrow -H_0(\boldsymbol{k})$. Without loss of generality, in the rest of this paper we deal with $0 < t_3 \leq t_1$. For the case $|t_1| \leq |t_3|$, the system can be thought as the case $|t_1| \geq |t_3|$ with the interchange of x and y axes, which is apparent in Fig. 1. For clarity, we list all possible band structure with $0 < t_3 \leq t_1$ in Fig. 2. The classification and topology of them will be discussed in the following.

A. Symmetry of The Eigenstates

$H_0(\boldsymbol{k})$ at time-reversal invariant momenta (TRIM)[26] can be solved analytically. The eigen energies, degeneracy and eigenvalue of symmetrical operators of the eigen states are listed in Table I. Little group at Γ of *Pbam* has only one-dimensional irreducible representations,[27] and all symmetrical operations can be diagonalized within the space spanned by eigen wave-functions.

At TRIM $X(\pi, 0, 0)$ or $Y(0, \pi, 0)$, *Pbam* has only 2D irreducible representations. Within

TABLE I: Eigen energies, their degeneracy and eigenvalues of symmetrical operations of $H_0(\boldsymbol{k})$ at four time-reversal invariant momenta (TRIM).

	Energy	Folds	$\mathcal{P}$	$\{C_{2x}\|\boldsymbol{\tau}_x\}$	$\{C_{2y}\|\boldsymbol{\tau}_y\}$
Γ	$E_A^0 = t_2 - 2(t_1 + t_3)$	1	1	-1	-1
	$E_B^0 = -t_2 - 2(t_1 - t_3)$	1	-1	-1	1
	$E_C^0 = -t_2 + 2(t_1 - t_3)$	1	-1	1	-1
	$E_D^0 = t_2 + 2(t_1 + t_3)$	1	1	1	1
X	$-\sqrt{t_2^2 + 4t_3^2}$	2	± 1	± 1	± 1
	$\sqrt{t_2^2 + 4t_3^2}$	2	± 1	± 1	± 1
Y	$-\sqrt{t_2^2 + 4t_1^2}$	2	± 1	± 1	± 1
	$\sqrt{t_2^2 + 4t_1^2}$	2	± 1	± 1	± 1
S	$-t_2$	2	$1, 1$	$\pm i$	$\pm i$
	t_2	2	$-1, -1$	$\pm i$	$\pm i$

the eigen states of $H_0(\boldsymbol{k})$, they can be written as following:

$$D_X(\mathcal{P}) = D_Y(\mathcal{P}) = \begin{pmatrix} \tau_3 & 0 \\ 0 & \tau_3 \end{pmatrix} \tag{12}$$

$$D_X\left(C_{2x}|\frac{1}{2}\frac{1}{2}0\right) = \begin{pmatrix} \tau_2 & 0 \\ 0 & \tau_2 \end{pmatrix} \tag{13}$$

$$D_Y\left(C_{2y}|\frac{1}{2}\frac{1}{2}0\right) = \begin{pmatrix} \tau_2 & 0 \\ 0 & \tau_2 \end{pmatrix} \tag{14}$$

in which τ_i denotes the i-th pauli matrix, representing the space spanned by two-fold degenerate eigenstates of $H_0(\boldsymbol{X})$ or $H_0(\boldsymbol{Y})$. We can character symmetry properties of each eigen space by eigenvalues of symmetrical operators. For example, the two-fold degenerate eigenstates at either X (or Y) have even and odd parities respectively since inversion symmetry $\mathcal{P}$ is represented as τ_3 (or τ_2), thus we note this eigen space with ± 1 in Table I. Solutions at $S(\pi, \pi, 0)$ are special. Little group of $Pbam$ at S has only one-dimensional irreducible representations. However, for $\{C_{2x}|\frac{1}{2}\frac{1}{2}0\}$ and $\{C_{2y}|\frac{1}{2}\frac{1}{2}0\}$, the eigenvalues of the two eigenstates with the same parity are $\pm i$. Thus, the TR operator connects them and makes them two-fold degenerate.
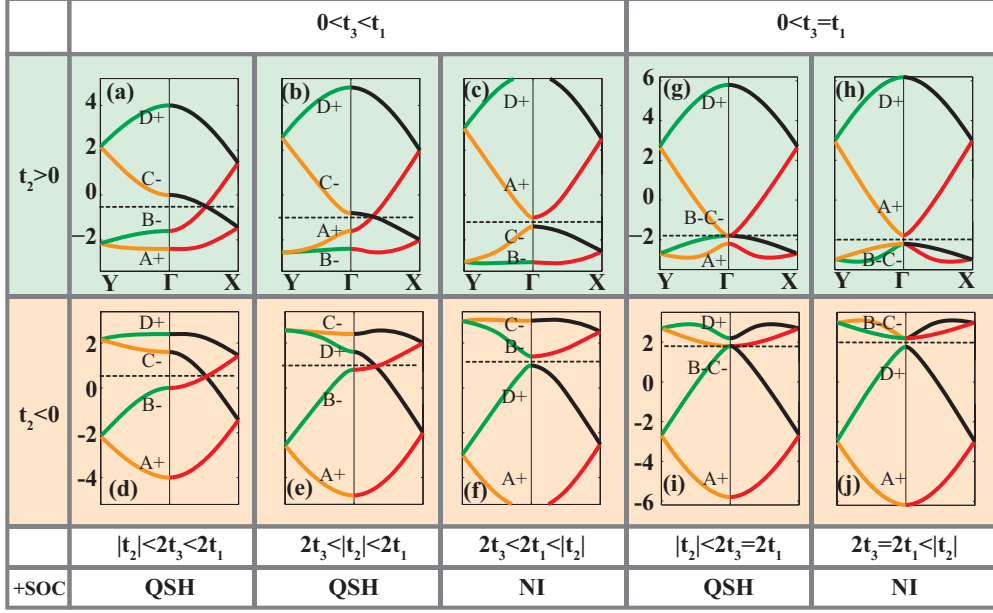
8

	$0<t_3<t_1$			$0<t_3=t_1$	
$t_2>0$	(a) D+, C-, B-, A+	(b) D+, C-, A+, B-	(c) D+, A+, C-, B-	(g) D+, B-C-, A+	(h) D+, A+, B-C-
$t_2<0$	(d) D+, C-, B-, A+	(e) C-, D+, B-, A+	(f) C-, B-, D+, A+	(i) D+, B-C-, A+	(j) B-C-, D+, A+
	$|t_2|<2t_3<2t_1$	$2t_3<|t_2|<2t_1$	$2t_3<2t_1<|t_2|$	$|t_2|<2t_3=2t_1$	$2t_3=2t_1<|t_2|$
+SOC	QSH	QSH	NI	QSH	NI

FIG. 2: Band structure of $H_0(\boldsymbol{k})$ for all possible parameter choices with $0 < t_3 \leq t_1$. (a)-(f) and (g)-(j) show bands without ($t_3 \neq t_1$) and with ($t_3 = t_1$) C_4 symmetry, respectively. Upper and lower panels are for $t_2 > 0$ and $t_2 < 0$ cases, respectively. Color of each band represents its representation under the conserved non-symmorphic rotational symmetry. Along Γ-X (Γ-Y), black (green) and red (yellow) represent +1 and -1 eigenvalue of $\{C_{2x}|\frac{1}{2}\frac{1}{2}0\}$ ($\{C_{2y}|\frac{1}{2}\frac{1}{2}0\}$), respectively. Including SOC term will drive the system into QSH insulator or normal insulator (NI) as indicated for different parameter choice.

From Table I, we can see that the order of eigen energies at X and Y do not depend on the choice of t_i. Further, since the parities of the double degenerate states are always in pair, the band inversion at X and Y will not change the topology of the occupied bands. At S, the situation is similar, though the energy order depends on sign of t_2. Therefore, only the band inversion at Γ can result in different topology of occupied bands. This is similar to large-band gap 2D topological insulator $ZrTe_5$.[17]

The order of energies at Γ depends on t_i explicitly as illustrated in Fig. 2. Along Γ-X(Y), $\{C_{2x}|\frac{1}{2}\frac{1}{2}0\}$ ($\{C_{2y}|\frac{1}{2}\frac{1}{2}0\}$) symmetry is conserved and the eigenstates with the same eigenvalue of $\{C_{2x}|\frac{1}{2}\frac{1}{2}0\}$ ($\{C_{2y}|\frac{1}{2}\frac{1}{2}0\}$) at different k points form a continuous band, which is identified by different color in Fig. 2. As long as $|t_2| < 2t_1$, the $\{C_{2x}|\frac{1}{2}\frac{1}{2}0\}$ eigenvalues of the two lower bands at Γ are $-1, -1$, while those at X are $1, -1$. There must be a level crossing along Γ-X path. However, if $|t_2| > 2t_1$, the eigenvalues of the two lower bands at Γ and X are

the same and so there is no crossing. But we'd like to remind that even without the above C_2 symmetry, as long as TR and $\mathcal{P}$ is conserved, such spineless 2D lattice model will have stable band crossing once band inversion happens.[28,29] C_2 symmetry constraints the crossing point on the path along Γ-X or Γ-Y, which is similar to the spinless graphene model.[3] A detailed discussion about these crossing points will be carried out in section IV.

B. Topological Phase

We now investigate whether a QSH insulating state can occur or not after SOC term is considered, which is similar to what happens in Kane-Mele model.[5,12] The $\mathbb{Z}_2$ number of system with both TR and inversion $\mathcal{P}$ symmetries is determined by the product of parities of occupied states at four TRIM.[26] SOC term opens band gap at the band crossing points as shown in Fig. 3(a). As long as $|t_2| < 2\max(t_1, t_3)$, $\mathbb{Z}_2$ number is 1 as shown in Fig. 2. To verify this we calculate the evolution of hybrid Wannier function centers for occupied bands using wilson loop method.[4,30] The plot is shown in Fig. 3(b). This illustrates that the winding number of two occupied bands is 1, indicating that the Chern number of spin up bands is 1. Due to TR symmetry, the spin down bands should have Chern number -1. Therefore, the model with $|t_2| < 2\max(t_1, t_3)$ and non-zero SOC parameter λ_i is a QSH insulator state. For the case $|t_2| > 2\max(t_1, t_3)$, there will be no band inversion and the product of parities is 1, i.e., the system becomes a trivial normal insulator (NI).

Explicitly, we investigate the topological phase transition (TPT) between TI and NI driven by tuning one parameter t_2. Such TPT from QSH insulator to NI in centrosymmetric system will experience a gapless state with a Dirac node at TRIM.[31,32] As illustrated in Fig. 2, the TPT can be thought as the bands inversion of A and C at Γ in case $t_2 > 0$ or B and D in case $t_2 < 0$. Hence, at TPT point the eigen energies of $H_0(\Gamma) + H_{so}(\Gamma)$ satisfy $E_A = E_C$ or $E_B = E_D$ with

$$E_A = t_2 - 2\sqrt{(t_1 + t_3)^2 + (\lambda_1 + \lambda_3)^2} \tag{15}$$

$$E_B = -t_2 - 2\sqrt{(t_1 - t_3)^2 + (\lambda_1 - \lambda_3)^2} \tag{16}$$

$$E_C = -t_2 + 2\sqrt{(t_1 - t_3)^2 + (\lambda_1 - \lambda_3)^2} \tag{17}$$

$$E_D = t_2 + 2\sqrt{(t_1 + t_3)^2 + (\lambda_1 + \lambda_3)^2}. \tag{18}$$

All of the corresponding eigen states are spin degenerate. It's easy to find the critical value
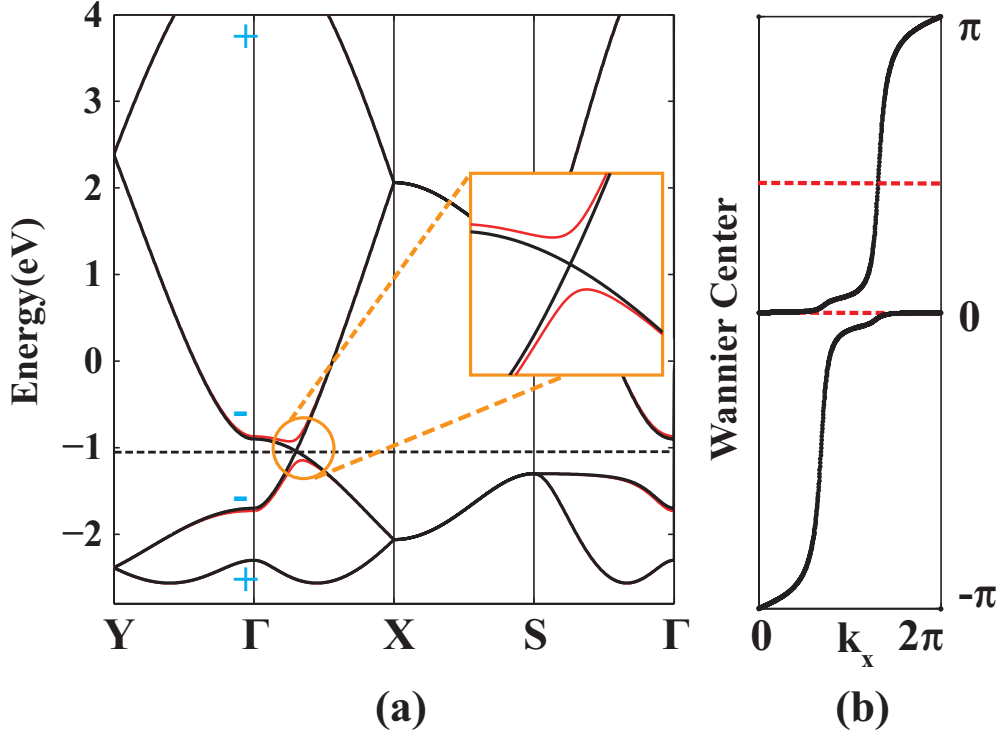
FIG. 3: Bands and wannier centers' evolution with SOC. (a) shows bands in which black lines denote non-SOC bands and red lines denote SOC bands. (b) shows wannier centers' evolution of spin up electrons. The dashed red lines indicate reference lines. The parameters are set as $t_1 = 1$, $t_2 = 1.3$, $t_3 = 0.8$, $\lambda_1 = -\lambda_3 = 0.04$.

of t_2:

$$t_{2C} = \pm \sqrt{(t_1 + t_3)^2 + (\lambda_1 + \lambda_3)^2}$$
$$\pm \sqrt{(t_1 - t_3)^2 + (\lambda_1 - \lambda_3)^2} \tag{19}$$

Since t_{2C} depends on t_i and λ_i (i=1 and 3), band inversion is influenced by both hopping effect and SOC in real materials.

IV. DIRAC POINTS AND QUADRATIC BAND TOUCHING

From the above discussion, our model can be looked as an analog of graphene on a rectangular lattice: a significant resemblance is that QSH state occurs when SOC term opens gap at Dirac points. Since the lattice constants a and b are quite close to each other in previously studied TMD haeckelites,[21] we'd like to go further to see what will happen
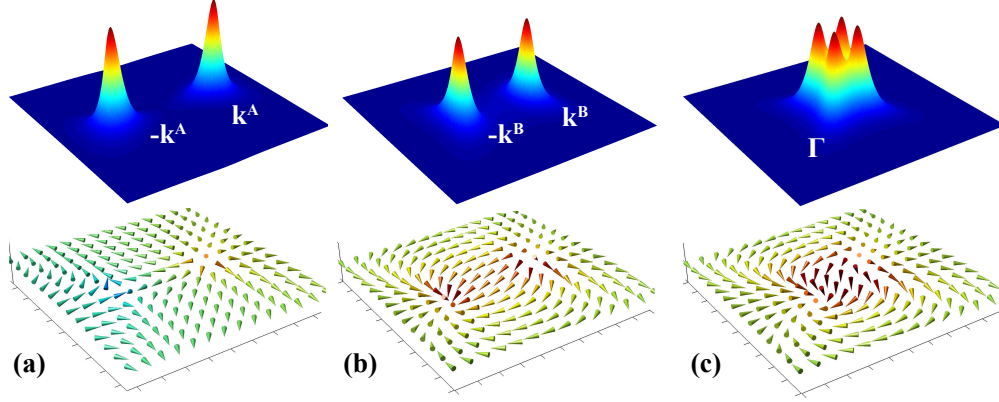
11

FIG. 4: Berry curvature and pseudospin distribution in momentum space around around band crossing or touching points. (a) shows the Dirac cones with opposite vorticity. (b) and (c) show the Dirac cones having the same vorticity when C_4 symmetry is slightly broken and conserved , respectively.

in a square lattice with C_4 symmetry, which is the case studied in Ref. 24 and 23. We find that in square lattice the non-SOC band structure has a quadratic band touching at Γ, being different from the linear Dirac cones in graphene and rectangular lattice. As all interesting physics are related to the linear Dirac cone or the quadratic non-Dirac cone band touching, in this section we use effective k·p model to characterize them. Alternatively, instead of calculating the evolution of centers of hybrid Wannier functions,[4,30] we calculate the integral of berry curvature analytically by treating H_{so} as an infinity small perturbation term to identify the topological invariant.

A.   Linear Dirac Nodes in Rectangular lattice

As the non-trivial topology comes from band inversion of A, C or B, D bands around Γ, it's natural to choose the states of A, C or B, D as the bases to establish k·p model to capture the essence of the underlying physics. We take the case of A, C band inversion in the following discussion and the B and D inversion case can be easily inferred from it. We expand Eq. (4) and Eq. (11) to second order of $\boldsymbol{k}$ and then use the downfolding technique[33,34] to reduce the dimensionality in order to get the effective Hamiltonian in the bases of eigenstates $|A\rangle$ and $|C\rangle$. To keep the k·p model similar to the Kane-Mele model, we transform $|A\rangle$ and

$|C\rangle$ to the following two bases:

$$|1\rangle = \frac{-|w_1\rangle + |w_4\rangle}{\sqrt{2}} \qquad |2\rangle = \frac{|w_2\rangle - |w_3\rangle}{\sqrt{2}} \qquad (20)$$

Within the above basis set, the space inversion and TR operators are

$$D_{AC}(\mathcal{P}) = \tau_1 \quad \text{and} \quad D_{AC}(K) = K \qquad (21)$$

, respectively, both of which are the same as those in Kane-Mele model.

After some approximation (neglecting second order of λ_i), we get the k·p model in basis set of $|1\rangle$ and $|2\rangle$:

$$H_{AC}(\boldsymbol{k}) = E_{AC}(\boldsymbol{k}) + \left[t_2 \left(2 - \frac{1}{8}\boldsymbol{k}^2 \right) - t_1 \left(2 - \frac{1}{4}k_x^2 \right) + Fk_x^2 \right] \tau_1 - \frac{t_2}{2}k_y\tau_2 + Jk_x\tau_3 \qquad (22)$$

$$F = \frac{t_2^2}{8(E_A - E_B)} - \frac{t_2^2}{8(E_C - E_D)} \qquad (23)$$

$$J = -\frac{t_2}{4} \left[\frac{\Delta_-}{E_A - E_B} + \frac{\Delta_-}{E_C - E_B} + \frac{\Delta_+}{E_A - E_D} + \frac{\Delta_+}{E_C - E_D} \right] \qquad (24)$$

where $E_{AC}(\boldsymbol{k})$ is an even function of $\boldsymbol{k}$ and $\Delta_\pm$ is defined as $\Delta_\pm = 2(\lambda_1 \pm \lambda_3)$.

If SOC is not present, i.e., $\Delta_\pm = 0$, there will be two Dirac cones from Eq. 22 and the location of the two nodes $\pm\boldsymbol{k}^A$ are determined by solution of $H_{AC}(\boldsymbol{k}) = 0$. $\boldsymbol{k}^A$ is found to be:

$$\boldsymbol{k}^A = \boldsymbol{e}_1\sqrt{\frac{2t_1 - t_2}{F + (2t_1 - t_2)/8}}. \qquad (25)$$

$\boldsymbol{e}_1$ is the unit vector along Γ-X path. In the case $t_1 < t_3$, $\boldsymbol{k}^A$ is along Γ-Y. Expanding the hamiltonian Eq. 22 around $\boldsymbol{k}^A$ or $-\boldsymbol{k}^A$ to the lowest order of $\Delta_\pm$ and $\boldsymbol{q}$ (here a general $\boldsymbol{k}$ is $\pm\boldsymbol{k}^A + \boldsymbol{q}$), we get a linear dispersion hamiltonian, i.e. a Dirac hamiltonian:

$$H(\pm\boldsymbol{k}^A + \boldsymbol{q}) = \pm\alpha k_1^A q_1\tau_1 - \frac{t_2}{2}q_2\tau_2 \pm Jk_1^A\tau_3 = \boldsymbol{d} \cdot \boldsymbol{\tau} \qquad (26)$$

$$\alpha = \frac{2t_1 - t_2}{4} + 2F \qquad (27)$$

Here $\boldsymbol{d} = (d_1, d_2, d_3)$ and $\boldsymbol{\tau} = (\tau_1, \tau_2, \tau_3)$. Representation of $\mathcal{P}K$ is $\tau_1 K$ and $(\mathcal{P}K)^{-1}H(\boldsymbol{k})\mathcal{P}K = H(\boldsymbol{k})$ guarantees the mass term (the term proportional to τ_3) to be zero. Therefore, $\boldsymbol{d}$ becomes a 2-component vector. The two Dirac cones possess opposite vorticity defined as sign(det($\partial\boldsymbol{d}/\partial\boldsymbol{q}$)). In this sense, any perturbation holds $\mathcal{P}K$ symmetry can only move the

positions of Dirac cones but can not annihilate them. This can also be easily seen from the texture of pseudospin, which is defined by pseudospin operator $\hat{\boldsymbol{\tau}}$, As shown in Fig. 4(a), the pseudospin of occupied state rotating 2π along an anticlockwise loop surrounding a Dirac cone gives a positive vorticity, while -2π gives a negative vorticity. Pseudospin rotates 0 along a loop containing the two Dirac cones and a trivial insulating state will be obtained when these two Dirac cones meet together.

In the presence of SOC term, the time reversal operator becomes $-i\sigma_y K$ which is different from K in spinless case. Hence complex conjugation symmetry is broken and a mass term is introduced which drives the system to QSH state as discussed above. Using the formula[2,8]:

$$\mathcal{F} = \frac{1}{2}\hat{\boldsymbol{d}} \cdot (\partial_{k_x}\hat{\boldsymbol{d}} \times \partial_{k_y}\hat{\boldsymbol{d}}) \tag{28}$$

where $\hat{\boldsymbol{d}} = \boldsymbol{d}/|\boldsymbol{d}|$, we calculate the berry curvature $\mathcal{F}$ around Dirac nodes:

$$\mathcal{F}_{AC}(\boldsymbol{q}) = \frac{\alpha t_2 J k_1^{A2}}{4\left(\alpha^2 k_1^{A2} q_1^2 + t_2^2 q_2^2/4 + J^2 k_1^{A2}\right)^{\frac{3}{2}}} \tag{29}$$

Integral of Eq. (29) around one Dirac point gives $\frac{1}{2}\text{sign}(\alpha t_2 J)$, thus the Chern number in spin up channel is 1 (or -1). Due to TR symmetry, spin Chern number would be 1 (or -1).

B. Quadratic Band Touching in Square Lattice with C_4 Symmetry

In this subsection, we will consider the square lattice with C_4 symmetry. This leads to $t_3 = t_1$ and $\lambda_3 = -\lambda_1$. Firstly, we consider $H_0(\boldsymbol{k})$ without SOC. As shown in Fig. 2g and 2i, there is gapless band touching at Γ and it is shown to be quadratic in the following discussion. This is due to the degeneracy of E_B and E_C at Γ and band inversion of E_A and E_C. If band inversion is absent, it becomes a trivial normal insulator as shown in Fig. 2h and 2j. These two cases are similar to zinc-blend HgTe with band inversion and CdTe without band inversion.[35]

Although the non-trivial topology comes from the A, C band inversion, the k·p model based on bands A and C can not reproduce the band touching at Fermi level because it comes from the degeneracy of B and C bands. Therefore, we construct a k·p model in bases of $|B\rangle$ and $|C\rangle$. To keep the similar form as H_{AC}, we also transform $|B\rangle$ and $|C\rangle$ to two new

14

bases:

$$|1\rangle = \frac{|w_1\rangle - i|w_2\rangle - |w_3\rangle + i|w_4\rangle}{2} \tag{30}$$

$$|2\rangle = \frac{i|w_1\rangle - |w_2\rangle - i|w_3\rangle + |w_4\rangle}{2} \tag{31}$$

Thus, the space inversion and complex conjugation operators are written as:

$$D_{BC}(\mathcal{P}) = -1 \qquad D_{BC}(K) = -i\tau_1 K \tag{32}$$

which is different from Eq. 21 and is responsible for the quadratic band touching. We get the Hamiltonian defined in basis set consisting of $|1\rangle$ and $|2\rangle$:

$$H_{BC}(\boldsymbol{k}) = -t_2\left(1 - \frac{1}{8}\boldsymbol{k}^2\right) + \left[t_3\left(2 - \frac{1}{4}k_y^2\right) - t_1\left(2 - \frac{1}{4}k_x^2\right)\right]\tau_1 + \frac{t_2}{4}k_x k_y \tau_2 + \Delta_- \tau_3 \tag{33}$$

Similar to the last subsection, by expanding the Hamiltonian around band touching points $\pm\boldsymbol{k}^B$ to the lowest order of $\Delta_\pm$ and $\boldsymbol{q}$, we get two Dirac cones:

$$H_{BC}(\pm\boldsymbol{k}^B + \boldsymbol{q}) = \pm\frac{t_1 k_1^B}{2}q_1\tau_1 \pm \frac{t_2 k_1^B}{4}q_2\tau_2 + \Delta_- \tau_3 \tag{34}$$

$$\boldsymbol{k}^B = \boldsymbol{e}_1\sqrt{8 - 8\frac{t_3}{t_1}} \tag{35}$$

If C_4 symmetry is slightly broken, the two linear Dirac cones are slightly separated by $2|\boldsymbol{k}^B|$. They are related by space inversion. However, because $\mathcal{P} = -1$ the two Dirac cones have the same vorticity. The pseudospin texture in Fig. 4(b) indicates the two Dirac cones have the same vorticity since pseudospin rotates 4π along an anticlockwise loop surrounding the two Dirac cones. This is the reason of quadratic band touching at Γ when C_4 symmetry brings these two Dirac cones together. Such quadratic band touching can also be seen from Eq. 33 by taking $t_3 = t_1$ and $\lambda_3 = -\lambda_1$ required by C_4 symmetry:

$$H_{BC}(\boldsymbol{k}) = E_{BC}(\boldsymbol{k}) + \frac{t_1}{4}(k_x^2 - k_y^2)\tau_1 + \frac{t_2}{4}k_x k_y \tau_2 + \Delta_- \tau_3 \tag{36}$$

where $E_{BC}(\boldsymbol{k})$ is an even function of $\boldsymbol{k}$.

Similarly, SOC breaks complex conjugation symmetry and introduces a non-zero mass and removes the above quadratic band touching degeneracy at Γ. This leads the system into insulator. To identify the band topology of this insulating state, the momentum distribution

of berry curvature around Γ can be calculated by Eq. (28):

$$\mathcal{F} = \frac{t_1 t_2 \Delta_- k^2}{4\sqrt{16\Delta_-^2 + k^4 \left[t_1^2 \cos^2(2\theta) + \frac{t_2^2}{4}\sin^2(2\theta)\right]}}$$

$$\theta = \arccos\left(\frac{k_x}{|\boldsymbol{k}|}\right)$$

(37)

It is shown in Fig. 4(c). The four-fold symmetrical distribution can be easily seen and understood from the 2θ terms. The integral of this berry curvature gives 1 (or -1). This indicates the Chern number in spin up channel is 1 (or -1) and the time-reversal symmetry ensures this insulating state to be a QSH insulator. As shown in Fig. 4(c), the two Dirac cones are now moved together to Γ to form a double Dirac cone,[36] and the pseudospin rotates 4π after adiabatic loop evolution surrounding it,[36] which indicates the quadratic band touching is non-trivial after H_{SO} is included.

V.   CONCLUSIONS

In this paper, we derived an low energy TB model for 2D TMD haeckelites MX_2-4-8 to uncover the physical mechanism controlling the topological phase transition. This square-like or rectangle lattice model contains only one orbital per site and four sites per unit cell. The band inversion is tuned by hopping parameters, which brings linear Dirac cones with the same or opposite vorticity. The annihilation or merging of them has been demonstrated through effective k·p model analysis and elaborated by pseudospin texture. SOC plays a critical role in opening band gap at the band crossing or band touching points, which drives the system into insulator. The hybrid Wannier function center evolution calculated by Wilson loop method, as well as the direct integral of Berry curvature, is used to identify the topology of insulating state. The QSH insulator can be obtained within reasonable parameter region and can be used to understand the band structures of TMD haeckelites MX_2-4-8 with M=Mo, W and X=S, Se, Te. Our model has extended the QSH lattice model family to square or rectangular lattice.

ACKNOWLEDGMENTS

---

[*] hmweng@iphy.ac.cn

[†] zfang@iphy.ac.cn

[1] M. Z. Hasan and C. L. Kane, Rev. Mod. Phys. **82**, 3045 (2010).

[2] X.-L. Qi and S.-C. Zhang, Rev. Mod. Phys. **83**, 1057 (2011).

[3] B. A. Bernevig and T. L. Hughes, *Topological Insulators and Topological Superconductors* (Princeton University Press, 2013).

[4] H. Weng, X. Dai, and Z. Fang, MRS Bulletin **39**, 849 (2014).

[5] C. L. Kane and E. J. Mele, Physical Review Letters **95**, 146802 (2005).

[6] B. A. Bernevig and S.-C. Zhang, Physical Review Letters **96**, 106802 (2006).

[7] L. Fu and C. L. Kane, Physical Review B **76**, 045302 (2007).

[8] X.-L. Qi, Y.-S. Wu, and S.-C. Zhang, Physical Review B **74**, 045125 (2006).

[9] X.-L. Qi, T. L. Hughes, and S.-C. Zhang, Phys. Rev. B **78**, 195424 (2008).

[10] M. K?nig, S. Wiedmann, C. Brne, A. Roth, H. Buhmann, L. W. Molenkamp, X.-L. Qi, and S.-C. Zhang, Science **318**, 766 (2007).

[11] I. Knez, R.-R. Du, and G. Sullivan, Physical Review Letters **107**, 136603 (2011).

[12] C. L. Kane and E. J. Mele, Physical Review Letters **95**, 226801 (2005).

[13] C.-C. Liu, W. Feng, and Y. Yao, Physical Review Letters **107**, 076802 (2011).

[14] Y. Xu, B. Yan, H.-J. Zhang, J. Wang, G. Xu, P. Tang, W. Duan, and S.-C. Zhang, Phys. Rev. Lett. **111**, 136804 (2013).

[15] C. Si, J. Liu, Y. Xu, J. Wu, B.-L. Gu, and W. Duan, Phys. Rev. B **89**, 115429 (2014).

[16] Z. Song, C.-C. Liu, J. Yang, J. Han, M. Ye, B. Fu, Y. Yang, Q. Niu, J. Lu, and Y. Yao, NPG Asia Materials **6**, e147 (2014).

[17] H. Weng, X. Dai, and Z. Fang, Physical Review X **4**, 011002 (2014).

[18] J.-J. Zhou, W. Feng, C.-C. Liu, S. Guan, and Y. Yao, Nano Letters **14**, 4767 (2014).

[19] X. Qian, J. Liu, L. Fu, and J. Li, Science **346**, 1344 (2014).

[20] W. Luo and H. Xiang, Nano Letters **15**, 3230 (2015).

[21] S. M. Nie, Z. Song, H. Weng, and Z. Fang, arXiv:1503.09040 [cond-mat.mtrl-sci] .

[22] Y. Sun, C. Felser, and B. Yan, ArXiv e-prints (2015), arXiv:1503.08460 [cond-mat.mtrl-sci].

[23] Y. Ma, L. Kou, Y. Dai, and T. Heine, ArXiv e-prints (2015), arXiv:1504.00197 [cond-mat.mtrl-sci].

[24] W. Li, M. Guo, G. Zhang, and Y.-W. Zhang, Phys. Rev. B **89**, 205402 (2014).

[25] H. Terrones and M. Terrones, 2D Materials **1**, 011003 (2014).

[26] L. Fu and C. L. Kane, Physical Review B **76**, 045302 (2007).

[27] M. I. Aroyo, A. Kirov, C. Capillas, J. M. Perez-Mato, and H. Wondratschek, Acta Crystallographica Section A **62**, 115 (2006).

[28] H. Weng, Y. Liang, Q. Xu, R. Yu, Z. Fang, X. Dai, and Y. Kawazoe, ArXiv e-prints (2014), arXiv:1411.2175 [cond-mat.mes-hall].

[29] R. Yu, H. Weng, Z. Fang, X. Dai, and X. Hu, ArXiv e-prints (2015), arXiv:1504.04577 [cond-mat.mtrl-sci].

[30] R. Yu, X. L. Qi, A. Bernevig, Z. Fang, and X. Dai, Phys. Rev. B **84**, 075119 (2011).

[31] S. Murakami and S.-i. Kuga, Physical Review B **78**, 165313 (2008).

[32] S. Murakami, Physica E **43**, 748 (2011).

[33] L. C. L. Y. Voon and M. Willatzen, *The k p Method: Electronic Properties of Semiconductors* (Springer Science & Business Media, 2009).

[34] R. Winkler, *Spin-orbit Coupling Effects in Two-Dimensional Electron and Hole Systems* (Springer Science & Business Media, 2003).

[35] B. A. Bernevig, T. L. Hughes, and S.-C. Zhang, Science **314**, 1757 (2006).

[36] G. Xu, H. Weng, Z. Wang, X. Dai, and Z. Fang, Physical Review Letters **107**, 186806 (2011).